Case Studies in Thermal Engineering 50 (2023) 103448

Contents lists available at ScienceDirect

Case Studies in Thermal Engineering

journal homepage: www.elsevier.com/locate/csite

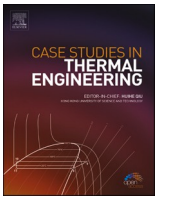

Heat transfer analysis of magnetized Cu-Ag-H_2O hybrid nanofluid radiative flow over a spinning disk when the exponential heat source and Hall current are substantial: Optimization and sensitivity analysis

Thirupathi Thumma [a], Devarsu Radha Pyari [c,d], Surender Ontela [b,c], Qasem M. Al-Mdallal [e,*], Fahd Jarad [f,g,**]

[a] Department of Computer Science, Vardhaman College of Engineering, Hyderabad, India
[b] Department of Mathematics, National Institute of Technology Kurukshetra, Haryana, 136119, India
[c] Department of Mathematics, National Institute of Technology Mizoram, Aizawl, 796012, India
[d] Department of Mathematics, Malla Reddy College of Engineering & Technology, Hyderabad, 500100, Telangana, India
[e] Department of Mathematical Sciences, UAE University, P.O. Box 15551, Al Ain, United Arab Emirates
[f] Department of Mathematics, Çankaya University, Ankara, 06790, Turkey
[g] Department of Medical Research, China Medical University, Taichung, 40402, Taiwan

ARTICLE INFO

Handling Editor: Huihe Qiu

Keywords:
Exponential space dependent heat source
Thermal radiation
Hybrid nanofluid flow
Spinning disk
Hall current
Response surface methodology
Sensitivity analysis

ABSTRACT

The main motive of the instigated mathematical model is to observe the impact of Hall current on the hybrid nanofluid flow over a disk that is rotating. The copper and silver metal nanoparticles have been considered with volume fraction $\varphi_1 = \varphi_2 = 0.01(0.01)0.04$ and are suspended in water to form the hybrid nanofluid. Diverse characteristics like magnetic field, thermal radiation, and (ESHS) exponential space dependent heat source are incorporated to investigate the nature of the flow. The present mathematical model is initiated with partial derivative equations (PDEs) which are redrafted as ordinary derivative equations (ODEs) with appropriate transformations of similarity. The results are attained through a blend of the Runge-Kutta method, shooting procedure, and the influences of parameters on the flow of nanofluid and hybrid nanofluid are compared and illustrated both as tables and graphs. The present numerical research is unique because by employing a complete quadratic CCD framework using the RSM strategy, the sensitivity and optimization analysis of the heat transmission improvement for the volume fraction, ESHS, and thermal radiation parameters have been performed. The R-squared and adjusted R-Squared are obtained as 100%. The residual graphs and contour diagrams of the same are also shown. The current study establishes that the Hall parameter increases the radial velocity, but it also controls the energy and cross-radial velocity. The rate of heat transmission is increased by thermal radiation even at low levels of ESHS. The rate of heat transmission is more sensitive (0.024670) to the volume fraction of the hybrid nanofluid when ESHS is at an intermediate level. The lowest sensitivity (-1.269967) value towards ESHS is observed For thermal radiation and ESHS parameter values, the heat transmission rate of the mono nanofluid is not as great as that of hybrid

* Corresponding author.
** Corresponding author. Department of Mathematics, Çankaya University, Ankara, 06790, Turkey.
E-mail addresses: thirupathi1706@vardhaman.org (T. Thumma), dpyari.math.phd@nitmz.ac.in (D.R. Pyari), surenderontela@nitkkr.ac.in (S. Ontela), q.almdallal@uaeu.ac.ae (Q.M. Al-Mdallal), fahd@cankaya.edu.tr (F. Jarad).

https://doi.org/10.1016/j.csite.2023.103448
Received 14 June 2023; Received in revised form 25 August 2023; Accepted 2 September 2023
Available online 4 September 2023

nanofluid. The current study finds applications in the generation of hydroelectric power, air cleansing and rotating equipment, healthcare devices, and many other industries.

Nomenclature

$(\widetilde{u},\widetilde{v},\widetilde{w})$	Velocity components
$(\widetilde{r},\varphi,\widetilde{z})$	Coordinate axes
B_0	Strength of the magnetic field
C_p	Specific heat
$\widetilde{T}$	Temperature
$\widetilde{T}_w$	Temperature at the surface
$\widetilde{T}_\infty$	Temperature at the free stream
k_{hnf}	Thermal conductivity of hybrid nanofluid
κ^*	Mean absorption coefficient
q_r	Rosseland radiative heat flux
Q_e	Exponential space-based heat source
n	Exponential index
M	Dimensionless Magnetic file parameter
m	Dimensionless Hall current parameter
Pr	Dimensionless Prandtl number
N	Dimensionless thermal radiation
Q_E	Dimensionless Exponential Space Based Heat Source
$\mathrm{Re}_{\widetilde{z}}$	Local Reynolds Number
$Cf_{\widetilde{r}}$	Local skin friction along a radial direction
$Cg_{\widetilde{r}}$	Local skin friction along a cross-radial direction
$Nu_{\widetilde{r}}$	Local Nusselt number

Greek Symbols

μ_{hnf}	Dynamic viscosity of hybrid nanofluid
ρ_{hnf}	Density of the hybrid nanofluid
σ_{hnf}	Electrical conductivity of the nanofluid
$(\rho C_p)_{hnf}$	Heat capacitance of the nanofluid
Ω	Angular velocity
ν_f	Kinematic viscosity of the fluid
σ^*	Stefan Boltzmann constant
φ	Volume fraction of the nanofluid
θ	Dimensionless temperature

1. Introduction

One kind of manufactured nanofluid (a colloidal suspension of nanoparticles) is the hybrid nanofluid, which contains nanoparticles from more than one different family. Two or more distinct nanoparticles, such as metal oxide or carbon nanotubes, are mixed in a single fluid to produce them. Heat transfer, medication delivery, and energy storage are just a few applications from the numerous applications existing for hybrid nanofluids. Hybrid nanofluids are desirable for application in thermal management systems because they outperform traditional fluids in several characteristics to list, some are viscosity, thermal conductivity, and heat capacity. To further improve efficiency and reduce costs, hybrid nanofluids may be modified to have the desired chemical or electrical characteristics. However, because the energy carried by a typical clean fluid is a bare minimum, many researchers were interested in exploring nanofluids and hybrid nanofluids in the twentieth century. Initiated by Choi and Eastman [1] in 1995, to develop energy-efficient heat transfer fluids, researchers started suspending nanoparticles into the base fluid. Later several research investigations reported that the resulting nanofluids and hybrid nanofluids tend to have enhanced thermal conductive abilities than the traditional fluid. Engaging the method of homotopy analysis, Algehyne et al. [2] proposed a semi-analytical approach to analyze the mixture of water and ethylene glycol in a fluid stream traveling through a rotating disc with heterogeneous and homogeneous processing. Gul et al. [3] used HAM to analyze the irreversibility of a hybrid CNT-couple stress nanofluid flowing subjected to an electromagnetic field, taking into account heat sources and sinks, as well as viscous and joule dissipation. In order to investigate the effects of the double diffusion Cattaneo Christov model and the Ota-Yamada model on the stream of a hybrid nanofluid flowing over a spinning disc, Upreti and Mishra [4] used the von-Karman similarity. For research purposes, Umair Khan et al. [5] examined how the

axisymmetric rotary stream of a fluid with the suspension of two different nanoparticles, past a revolving porous disc was influenced by the existence of Maxwell momentum slip and Smoluchowski temperature constraints. Some of the literature supporting the enhanced thermal conductivity based on the various conditions like size, shape, material, medium, geometry et cetera in the later fluids and their applications may be referred from Refs. [6–10] and others.

A voltage is engendered across a material when a current flows through it, crossways to a magnetic field, in an impression called the Hall effect. This consequence is used to appraise the magnitude and trajectory of a magnetic field, as well as to measure current in the proximity of a magnetic field. It is used in many scenarios, such as magnetic sensors to evaluate the placement of an article, magnetic switches, and current discernment gadgets. Several researchers have admitted to exploring the Hall current effects owing to their obvious usefulness. Which includes, controlling the temperature of the nanofluid, controlling the flow rate, and creating an electric field to induce particle separation. In the flow of a rotating unsteady dissipative nanofluid, Khan et al. [11] quantitatively investigated the impression of the hall current using radiative heat flux by utilizing a collocation approach. According to their research, the volume percentage of a hybrid nanofluid controls the rate of transmission of heat. Considering the hall current and thermal radiation impact, Shamshuddin et al. [12] explored the transition of energy involved to improve heat transport of a ternary hybrid nanofluid flowing across the surface of a disc that is spinning. The impacts of thermophysical parameters (viscosity, density, and thermal conductivity) and Hall parameters were studied by Shehzad et al. [13] in a viscous fluid with a laminar flow that is unstable, compressible, and exhibiting a laminar shear layer. Elattar et al. [14] proposed a computational model to improvise the performance and productivity of thermal energy of a fluid suspended with two types of nanoparticles streaming across a stretchable sheet considering the influences of chemical reactions, heat generation, magnetic field, and Hall parameter. There are some more references on the study of the hall current parameter and how it influences the current of hybrid nanofluids [15–17].

A spinning (or revolving) item submerged in the fluid has a variety of applications in technology that include mixing systems and gearbox lubrication. The simplest fundamental issue of this type is the flow of a spinning/revolving disc. The application of spinning discs has important implications for heat transfer enhancement in diverse renewable energy systems and equipment of industrial thermal management. Mousavi et al. [18] used Temperature-dependent experimentally based thermal conductivity to regulate the current of a fluid comprising of zinc oxide, silver, and water (HNF) toward an off-center spinning disc by employing HAM. In a recent study, Waini et al. [19] studied the deceleration and suction effects of an HNF streaming above a spinning disc. Also, the long-term stability of the various solutions is explored and the results reveal that many solutions are verifiable under particular operational conditions. Examination of a hybrid nanofluid's MHD flow induced by a decelerating spinning disc with Dufour, Soret, and Ohmic heating effects was performed by Vijay et al. [20], who employed the Maple's Midrich BVP scheme to illustrate the characteristics of emergent non-dimensional parameters. Acharya et al. [21] used the RK technique and shooting procedure to study the generation of entropy of the hybrid nanofluid running on a rotating disc, taking into account velocity slips, magnetic influence, and radiation effects. It was suggested that using magnetic spinning discs in nuclear propulsion, space engines, and other applications may have significant numerical repercussions. Further research on spinning discs can be found in Refs. [22–25].

A type of heat source that produces a temperature profile that follows an exponential decay curve is known as an exponential heat source. In a hybrid nanofluid circulating over a revolving disc, this source of heat is frequently embedded. In this setup, an exponential heat source heats a spinning disc, and nanofluid is pumped through the disc to help dissipate the heat. The temperature profile of the disc follows an exponential decay curve, which means that the temperature decreases exponentially as one moves away from the disk's center. The use of a nanofluid in conjunction with an exponential heat source allows for efficient heat dissipation from the disk, making it an ideal setup for applications such as cooling electronics. In the process of analyzing the convective boundary layer flow of a fluid blended with three types of nanoparticles across a curvy stretched sheet with stimulation of energy, Sarada et al. [26] considered the heat flux non-Fourier model. In addition to discussing the effects of an exponential heat source and Joule dissipation, Swain et al. [27] also explored the magnetic strength impact proportional to Lorentz force on such changing aspects based on the model of nanofluids. Ullah et al. [28] discussed how radiation, exponential heat source, and hall current impact the important characteristics of varying permeability and porosity on hybrid nanofluid circulating through Darcy-Forchheimer space above an axis-spinning disc. Using Von-Karman stretching transformations, Mahanthesh et al. [29] examined the heat-transmitting properties of nanofluid streaming over a rotating disc in the existence of convective boundary conditions and an applied magnetic field. Multiple researches have been executed to understand the impact of a space dependent heat source rising exponentially on nano or hybrid nanofluids, some of those may be referred to in Refs. [30–33].

The process of designing experiments is an integral part of many scientific and commercial endeavors. It requires treating experimental units to measure a response. One of the most popular optimization experiments uses a technique called response surface methodology (RSM). This method uses mathematics and statistics to investigate how various factors influence the response of interest to produce the greatest possible result. In general, analysis of variance is used to examine the correctness of the model utilizing the response surface methodology (RSM). The degrees of freedom (DOF), modified mean squares, sum of squares, F, and p values are calculated during this process as statistical estimators. It's vital to remember that the F-value determines how far the data varies from its mean. The accuracy of the input data can be justified if F-values are greater than one. As a result, the F-value is sufficient for controlling needs. The P-values are then used to determine the model's statistical significance. The Response Surface Methodology (RSM) is a practical technique for observing the correct mechanism and calculating the input parameter values that maximize the response. Recently, numerous RSM investigations have been carried out; some of these can be explored in Refs. [34–37]. Mehmood et al. [38] examined a magnetohydrodynamic fluid containing a new mix of carbon nanotubes that are multi-walled in motor oil passing through a stretchable revolving disc and solved it using numerical bvp4c algorithm and also implemented the response surface technique to complete the study. It is demonstrated that the local Nusselt number and the surface drag coefficient respond constructively to the nanoparticle's volume fraction. It is adversely affected by the Magnetic parameter. Rana et al. [39] employed the

Cattaneo-Christov Theory to simulate the heat flux influence on a nanofluid flowing on a spinning disc and examined the heat transport sensitivity. In their investigation, ideal levels of Eckert number, Hartmann number, and Hall parameter that maximize heat transport are identified, and concluded that the Lorentz force plays a major role in amplifying the thermal layer structure resulting in the system's heat transit diminishing. Also, the parameter of Hall current upsurges the velocity layer thickness in the radial direction while diminishing the heat layer thickness. Adam's Bashforth corrector-predictor methodology was used by Hussain et al. [40] to study the sensitivity through the response surface procedure of magnetohydrodynamic nano liquid flow on a surface stretching exponentially considering unstable heat flux. They concluded that the Biot number and the coefficients of surface drag, and local heat transfer rate are more sensitive than the nanoparticle volume percent and magnetic field parameter.

A thorough examination has been conducted in light of the cited publications. As per the awareness of authors, recently, little attention has been paid to the analyzing optimization and sensitivity of the exponentially increasing heat source and thermal radiation parameter on the flow of hybrid nanofluids. Hence, the uniqueness of the current numerical investigation is the optimization and sensitivity analysis on the significance of independent factors in improving the rate of heat transmission using the response surface method and examining the influence of ESHS as well as the volume fraction of hybrid nanofluid effects on boundary layer profiles. The resulting boundary layer flow balance nonlinear PDEs are altered into a system of ODEs and explored numerically by employing Runge Kutta Scheme in conjunction with Shooting Procedure. Therefore, important outcomes of the evaluation could include:

- How would the magnetic parameter affect the radial, and cross-radial velocities, and temperature?
- What effects does the rising solid volume fraction have on the momentum of the fluid and energy transport near the boundary layer and Nusselt number?
- What impact do the radiation parameter and the exponentially growing heat source in space have on the temperature?
- In what ranges do the various variables play a role in determining the optimal response?
- When the independent variables are at what levels do the response functions become more sensitive to the factors?

2. Mathematical formulation of the problem statement

An incompressible steady hybrid nanofluid flowing over a non-conducting axis-spinning disk placed at $\widetilde{z}=0$ and revolving about $\widetilde{z}-$ axis with invariable angular velocity Ω is considered. Let the strength of the magnetic field perpendicular to the disk be B_0, disk temperature at the surface be $\widetilde{T}_w$ and disk temperature away from the surface be $\widetilde{T}_\infty$ respectively. The flow configuration is depicted in Fig. 1.

Mentioning some parameters of the hybrid nanofluid: pressure as p, temperature as $\widetilde{T}$, density as ρ_{hnf}, dynamic viscosity as μ_{hnf}, Hall current parameter as m, thermal conductivity as κ_{hnf} specific heat as $(\rho C_p)_{hnf}$, radiative heat flux as q_r , and velocity components are denoted as $(\widetilde{u},\widetilde{v},\widetilde{w})$ along the directions of the three axes respectively. Assuming that the nanoparticles and the base fluid do not react chemically, maintain thermal equilibrium and the absence of slip within the nanoparticles. It also assumed that the induced electrical and magnetic fields as well as viscous and joule dissipation effects are ignored. Thus, the mathematical formulation (following Acharya et al. [41])for the considered flow is developed in the cylindrical co-ordinate scheme $(\widetilde{r},\varphi,\widetilde{z})$ as follows:

$$\frac{\partial\widetilde{u}}{\partial\widetilde{r}}+\frac{\widetilde{u}}{\widetilde{r}}+\frac{\partial\widetilde{w}}{\partial\widetilde{z}}=0 \tag{1}$$

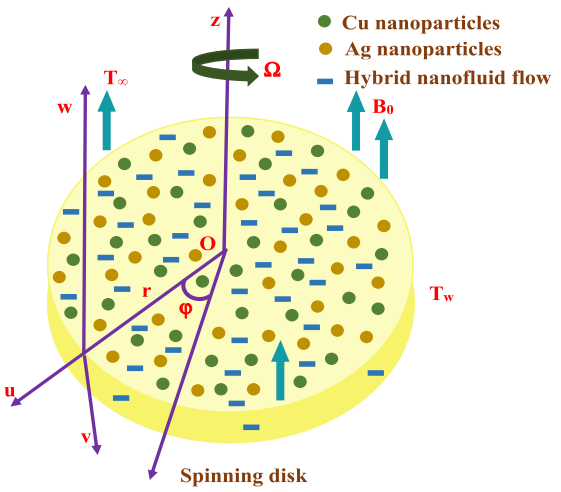

Fig. 1. Schematic hybrid nanofluid flow diagram.

$$\rho_{hnf}\left(\widetilde{u}\frac{\partial\widetilde{u}}{\partial\widetilde{r}}-\frac{\widetilde{v}^2}{\widetilde{r}}+\widetilde{w}\frac{\partial\widetilde{u}}{\partial\widetilde{z}}\right)+\frac{\partial p}{\partial\widetilde{r}}=\mu_{hnf}\left(\frac{\partial^2\widetilde{u}}{\partial\widetilde{r}^2}+\frac{1}{\widetilde{r}}\frac{\partial\widetilde{u}}{\partial\widetilde{r}}-\frac{\widetilde{u}}{\widetilde{r}^2}+\frac{\partial^2\widetilde{u}}{\partial\widetilde{z}^2}\right)-\frac{\sigma_{hnf}{B_0}^2}{(1+m^2)}(\widetilde{u}-m\widetilde{v}) \tag{2}$$

$$\rho_{hnf}\left(\widetilde{u}\frac{\partial\widetilde{v}}{\partial\widetilde{r}}-\frac{\widetilde{u}\widetilde{v}}{\widetilde{r}}+\widetilde{w}\frac{\partial\widetilde{v}}{\partial\widetilde{z}}\right)=\mu_{hnf}\left(\frac{\partial^2\widetilde{v}}{\partial\widetilde{r}^2}+\frac{1}{\widetilde{r}}\frac{\partial\widetilde{v}}{\partial\widetilde{r}}-\frac{\widetilde{v}}{\widetilde{r}^2}+\frac{\partial^2\widetilde{v}}{\partial\widetilde{z}^2}\right)-\frac{\sigma_{hnf}{B_0}^2}{(1+m^2)}(\widetilde{v}+m\widetilde{u}) \tag{3}$$

$$\rho_{hnf}\left(\widetilde{u}\frac{\partial\widetilde{w}}{\partial\widetilde{r}}+\widetilde{w}\frac{\partial\widetilde{w}}{\partial\widetilde{z}}\right)+\frac{\partial p}{\partial\widetilde{z}}=\mu_{hnf}\left(\frac{\partial^2\widetilde{w}}{\partial\widetilde{r}^2}+\frac{1}{\widetilde{r}}\frac{\partial\widetilde{w}}{\partial\widetilde{r}}+\frac{\partial^2\widetilde{w}}{\partial\widetilde{z}^2}\right) \tag{4}$$

$$\left(\rho C_p\right)_{hnf}\left(\widetilde{u}\frac{\partial\widetilde{T}}{\partial\widetilde{r}}+\widetilde{w}\frac{\partial\widetilde{T}}{\partial\widetilde{z}}\right)=k_{hnf}\left(\frac{\partial^2\widetilde{T}}{\partial\widetilde{r}^2}+\frac{1}{\widetilde{r}}\frac{\partial\widetilde{T}}{\partial\widetilde{r}}+\frac{\partial^2\widetilde{T}}{\partial\widetilde{z}^2}\right)-k_{hnf}\frac{\partial q_r}{\partial\widetilde{z}}+(\widetilde{T}_w-\widetilde{T}_\infty)Q_e\exp\left(-n\sqrt{\frac{2\Omega}{\nu_f}}\widetilde{z}\right) \tag{5a}$$

where using Rosseland approximation the heat flux for radiation is simplified as $q_r=-\frac{4\sigma^*}{3\kappa^*}.\frac{\partial\widetilde{T}^4}{\partial\widetilde{z}}$, (6a)

Here Taylor series is employed to expand $\widetilde{T}^4$ as $\widetilde{T}^4\approx 4\widetilde{T}.\widetilde{T}_\infty{}^3-3\widetilde{T}_\infty{}^3$ the higher order terms and gives,

$$\frac{\partial q_r}{\partial\widetilde{z}}=-\frac{4\sigma^*}{3\kappa^*}4\widetilde{T}_\infty^3\frac{\partial^2\widetilde{T}}{\partial\widetilde{z}^2}, \tag{6b}$$

In view of Eqn. (6b) into Eqn. (5a), we get

$$\begin{aligned}\left(\rho C_p\right)_{hnf}\left(\widetilde{u}\frac{\partial\widetilde{T}}{\partial\widetilde{r}}+\widetilde{w}\frac{\partial\widetilde{T}}{\partial\widetilde{z}}\right)&=k_{hnf}\left(\frac{\partial^2\widetilde{T}}{\partial\widetilde{r}^2}+\frac{1}{\widetilde{r}}\frac{\partial\widetilde{T}}{\partial\widetilde{r}}+\frac{\partial^2\widetilde{T}}{\partial\widetilde{z}^2}\right)+\frac{16\sigma^*}{3\kappa^*}\widetilde{T}_\infty^3\frac{\partial^2\widetilde{T}}{\partial\widetilde{z}^2}\\&+(\widetilde{T}_w-\widetilde{T}_\infty)Q_e\exp\left(-n\sqrt{\frac{2\Omega}{\nu_f}}\widetilde{z}\right)\end{aligned} \tag{5b}$$

Subject to the conditions

$$\left.\begin{array}{c}\widetilde{u}=0,\widetilde{v}=\Omega\widetilde{r},\widetilde{w}=0,\widetilde{T}=\widetilde{T}_w\text{ at }\widetilde{z}=0,\\\text{and}\\\widetilde{u}\to 0,\widetilde{v}\to 0,\widetilde{T}=\widetilde{T}_\infty,P=P_\infty\text{ at }\widetilde{z}\to\infty.\end{array}\right\} \tag{7}$$

The present study is conducted jointly for nanofluid *Ag* - H_2O and hybrid nanofluid *Cu-Ag-*H_2O. The thermophysical model equations to acquire the flow features accurately for the nanofluid and hybrid nanofluid are defined as prescribed by Acharya et al. [41] These formulations are depicted in Table 1 and Table 2 respectively. The thermophysical data of tiny particles are listed in Table 3. It is important to note that inserting $\varphi_{Cu}=0.0$ reduces to nanofluid as mentioned by Oztop et al. [42].

where each of the subscripts stands for base fluid - *f*, nanofluid - *nf*, hybrid nanofluid - *hnf*, *Cu* nanoparticles – s_1, *Ag* nanoparticles – s_2, φ_{Cu} and φ_{Ag} the considered solid's volume fractions, viscosity of the base fluid - μ_f, the densities of each nanofluid and base fluid are ρ_s and ρ_f, the specific heat parameters of the nanoparticles and base fluid are $(\rho C_p)_s$ and $(\rho C_p)_f$, the thermal conductivities of the nanoparticles and base fluid are κ_s and κ_f respectively.

The mathematical formulations of the flow are converted into dimensionless form through the following (See Acharya et al. [41]) similarity conversions

Table 1
Thermophysical Properties of $Cu-Ag-H_2O$ (Hybrid Nanofluid) (See Acharya et al. [41]).

Properties	Hybrid nanofluid $(Cu-Ag-H_2O)$
Thermal Conductivity	$\frac{k_{Cu-Ag-H_2O}}{k_{Ag-H_2O}}=\frac{k_{Ag}+(n-1)k_{Ag-H_2O}-(n-1)\varphi_{Ag}(k_{Ag-H_2O}-k_{Ag})}{k_{Ag}+(n-1)k_{Ag-H_2O}+\varphi_{Ag}(k_{Ag-H_2O}-k_{Ag})}$ where $\frac{k_{Ag-H_2O}}{k_{H_2O}}=\frac{k_{Cu}+(n-1)k_{H_2O}-(n-1)\varphi_{Cu}(k_{H_2O}-k_{Cu})}{k_{Cu}+(n-1)k_{H_2O}+\varphi_{Cu}(k_{H_2O}-k_{Cu})}$
Viscosity	$\mu_{Cu-Ag-H_2O}=\frac{\mu_{H_2O}}{(1-\varphi_{Cu})^{2.5}(1-\varphi_{Ag})^{2.5}}$
Electrical Conductivity	$\frac{\sigma_{Cu-Ag-H_2O}}{\sigma_{Ag-H_2O}}=\frac{\sigma_{Ag}+2\sigma_{Ag-H_2O}-2\varphi_{Ag}(\sigma_{Ag-H_2O}-\sigma_{Ag})}{\sigma_{Ag}+2\sigma_{Ag-H_2O}+\varphi_{Ag}(\sigma_{Ag-H_2O}-\sigma_{Ag})}$ where $\frac{\sigma_{Ag-H_2O}}{\sigma_{H_2O}}=\frac{\sigma_{Cu}+2\sigma_{H_2O}-2\varphi_{Cu}(\sigma_{H_2O}-\sigma_{Cu})}{\sigma_{Cu}+2\sigma_{H_2O}+\varphi_{Cu}(\sigma_{H_2O}-\sigma_{Cu})}$
Heat Capacity	$(\rho C_p)_{Cu-Ag-H_2O}=\{(1-\varphi_{Ag})[(1-\varphi_{Cu})(\rho C_p)_{H_2O}+\varphi_{Cu}(\rho C_p)_{Cu}]\}+\varphi_{Ag}(\rho C_p)_{Ag}$
Density	$\rho_{Cu-Ag-H_2O}=\{(1-\varphi_{Ag})[(1-\varphi_{Cu})\rho_{H_2O}+\varphi_{Cu}\rho_{Cu}]\}+\varphi_{Ag}\rho_{Ag}$

Table 2
Thermophysical Properties of $Ag-H_2O$ (Nanofluid)(See Acharya et al. [41]).

Properties	Nanofluid $(Ag-H_2O)$
Thermal Conductivity	$\frac{k_{Ag-H_2O}}{k_{H_2O}} = \frac{k_{Ag}+(n-1)k_{H_2O}-(n-1)\varphi_{Ag}(k_{H_2O}-k_{Ag})}{k_{Ag}+(n-1)k_{H_2O}+\varphi_{Ag}(k_{H_2O}-k_{Ag})}$
Viscosity	$\mu_{Ag-H_2O} = \frac{\mu_{H_2O}}{(1-\varphi_{Ag})^{2.5}}$
Electrical Conductivity	$\frac{\sigma_{Ag-H_2O}}{\sigma_{H_2O}} = 1+\frac{3(\sigma-1)\varphi_{Ag}}{(\sigma+2)-(\sigma-1)\varphi_{Ag}}$ where $\sigma = \frac{\sigma_{Ag}}{\sigma_{H_2O}}$
Heat Capacity	$(\rho C_p)_{Ag-H_2O} = (1-\varphi_{Ag})(\rho C_p)_{H_2O} + \varphi_{Ag}(\rho C_p)_{Ag}$
Density	$\rho_{Ag-H_2O} = (1-\varphi_{Ag})\rho_{H_2O} + \varphi_{Ag}\rho_{Ag}$

Table 3
Thermophysical properties of $Ag-H_2O-Cu$

Physical Properties	Silver (Ag)	Water (H_2O)	Copper (Cu)
$\sigma(s/m)$	6.3×10^7	5.5×10^{-6}	5.96×10^7
$k(W/mK)$	429	0.613	401
$C_p(J/KgK)$	235	4179	385
$\rho(Kg/m^3)$	10500	997.1	8933

$$\left.\begin{aligned} \widetilde{u} = \widetilde{r}\Omega f', \widetilde{v} = \widetilde{r}\Omega g, \widetilde{w} = -\sqrt{2\Omega\nu_f}f, \theta(\eta) = \frac{\widetilde{T}-\widetilde{T}_\infty}{\widetilde{T}_w-\widetilde{T}_\infty}, \\ P = P_\infty + 2\Omega\mu_f P(\eta), \eta = \sqrt{\frac{2\Omega}{\nu_f}}\widetilde{z} \end{aligned}\right\} \tag{8}$$

where η is the similarity variable.

Using (8), the governing equations (1) to (4) and (5b) along with (7) become

$$2f''' + \frac{\left(\frac{\rho_{Cu-Ag-H_2O}}{\rho_{H_2O}}\right)}{\left(\frac{\mu_{Cu-Ag-H_2O}}{\mu_{H_2O}}\right)}\left(2ff'' - f'^2 + g^2\right) - \frac{\left(\frac{\sigma_{Cu-Ag-H_2O}}{\sigma_{H_2O}}\right)}{\left(\frac{\mu_{Cu-Ag-H_2O}}{\mu_{H_2O}}\right)}\frac{M}{(1+m^2)}(f'-mg) = 0 \tag{9}$$

$$2g'' + \frac{\left(\frac{\rho_{Cu-Ag-H_2O}}{\rho_{H_2O}}\right)}{\left(\frac{\mu_{Cu-Ag-H_2O}}{\mu_{H_2O}}\right)}(2fg' - 2f'g) - \frac{\left(\frac{\sigma_{Cu-Ag-H_2O}}{\sigma_{H_2O}}\right)}{\left(\frac{\mu_{Cu-Ag-H_2O}}{\mu_{H_2O}}\right)}\frac{M}{(1+m^2)}(g+mf') = 0 \tag{10}$$

$$\frac{1}{\Pr}\theta''\left(\frac{k_{Cu-Ag-H_2O}}{k_{H_2O}}+\frac{4N}{3}\right) + \frac{(\rho C_p)_{Cu-Ag-H_2O}}{(\rho C_p)_{H_2O}}f\theta' + Q_E e^{-m\eta} = 0 \tag{11}$$

Similarly, the transformed boundary conditions can be noted as

$$\left.\begin{aligned} f = 0, f' = 0, g = 1, \theta = 1 \text{ at } \eta = 0 \\ f'\to 0, g\to 0, \theta\to 0 \text{ as } \eta\to\infty \end{aligned}\right\} \tag{12}$$

The dimensionless factors are listed below:

$$\left.\begin{aligned} &\text{Prandtl number, } \Pr = \frac{\mu_{H_2O}(\rho C_p)_{H_2O}}{\rho_{H_2O}k_{H_2O}}, \\ &\text{Radiation parameter, } N = \frac{4\sigma^* {T_\infty}^3}{k^* k_{H_2O}} \\ &\text{Magnetic parameter, } M = \frac{\sigma_{H_2O}{B_0}^2}{\rho_{H_2O}\Omega} \\ &\text{ESHS parameter, } Q_E = \frac{Q_e}{2\Omega(\rho C_p)_{H_2O}} \end{aligned}\right\} \tag{13}$$

Table 4
Validation of the numerical results when $Q_E = 0$.

	Acharya et al. [41]	Present Results
$-\theta'(0)$	0.9338728	0.93387286
$-g'(0)$	0.6159197	0.61591968
$f'(0)$	0.5102295	0.51022947

Surface drag (Skin friction) and the heat transfer rate (Nusselt number) are physical characteristics that are essential in order to construct engineering equipment at the nanoscale. They are presented mathematically as:

$$\left.\begin{aligned} &Cf = \frac{\tau_{w1}}{\rho_{H_2O}(\tilde{r}\Omega)^2}, Cg = \frac{\tau_{w2}}{\rho_{H_2O}(\tilde{r}\Omega)^2}, Nu = \frac{\tilde{r}q_w}{k_{H_2O}(\tilde{T}_w - \tilde{T}_\infty)}, \\ &\tau_{w1} = \mu_{Cu-Ag-H_2O}\left(\frac{\partial\tilde{u}}{\partial\tilde{z}}\right)_{\tilde{z}=0}, \tau_{w2} = \mu_{Cu-Ag-H_2O}\left(\frac{\partial\tilde{v}}{\partial\tilde{z}}\right)_{\tilde{z}=0} \text{ and } q_w = -k_{Cu-Ag-H_2O}\left(\frac{\partial\tilde{T}}{\partial\tilde{z}}\right)_{\tilde{z}=0} + q_r|_{\tilde{z}=0} \end{aligned}\right\} \tag{14}$$

The reduced skin friction and reduced Nusselt number are obtained as the modified versions of (14) by applying the dimensionless transformations as in (8), respectively are:

$$Cf_{\tilde{r}} = \sqrt{\mathrm{Re}_{\tilde{z}}}.Cf = \frac{f''(0)}{\sqrt{2}(1-\varphi_{Cu})^{2.5}.(1-\varphi_{Ag})^{2.5}} \tag{15}$$

$$Cg_{\tilde{r}} = \sqrt{\mathrm{Re}_{\tilde{z}}}.Cg = \frac{g'(0)}{\sqrt{2}(1-\varphi_{Cu})^{2.5}.(1-\varphi_{Ag})^{2.5}} \tag{16}$$

$$Nu_{\tilde{r}} = \frac{Nu}{\sqrt{\mathrm{Re}_{\tilde{z}}}} = -\sqrt{2}\left(\frac{k_{Cu-Ag-H_2O}}{k_{H_2O}} + \frac{4N}{3}\right)\theta'(0) \tag{17}$$

where $\mathrm{Re}_{\tilde{z}} = \dfrac{\tilde{r}^2\Omega}{\nu_{H_2O}}$ represents local Reynolds number.

The governing equations (9) to (11) are nonlinear and have related boundary requirements (12). So, utilizing the Runge-Kutta-4th ordered technique with the shooting technique, the required equations with boundary condition (12) are solved. Initially, the leading equations are transformed into a system of first-order ODEs, and then step-by-step integration is carried out using the RK-4 approach with shooting criteria. The entire set of numerical results is produced with MATLAB. The $\eta = \eta_\infty$ boundary conditions take the place of the $\eta \to \infty$ boundary conditions. In every instance, the convergence criteria 10^{-6} are used for the inner iteration.

To ensure the validity of the current study, the values of $-\theta'(0), -g'(0), f'(0)$ being equated with the values published by Acharya et al. [41], assuming $M = m = N = \varphi_1 = \varphi_2 = 0$ and $\mathrm{Pr} = 6.2$ in Table 4 and the results are in perfect pact with the known literature.

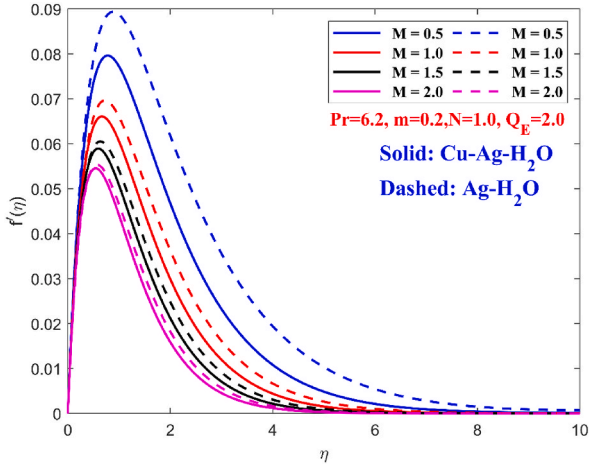

Fig. 2. Outcome of magnetic parameter on radial velocity.

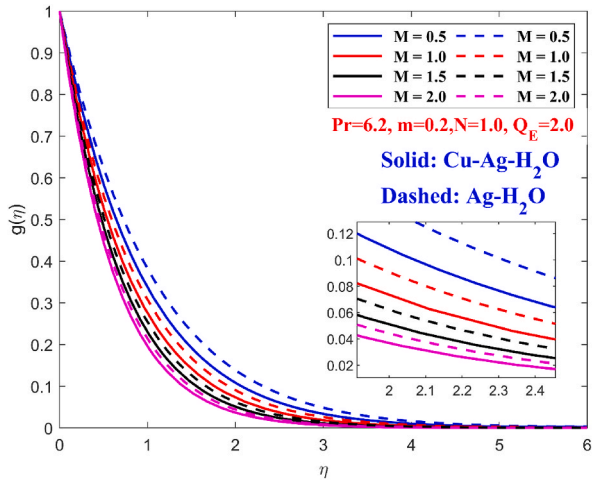

Fig. 3. Outcome of magnetic parameter on cross-radial velocity.

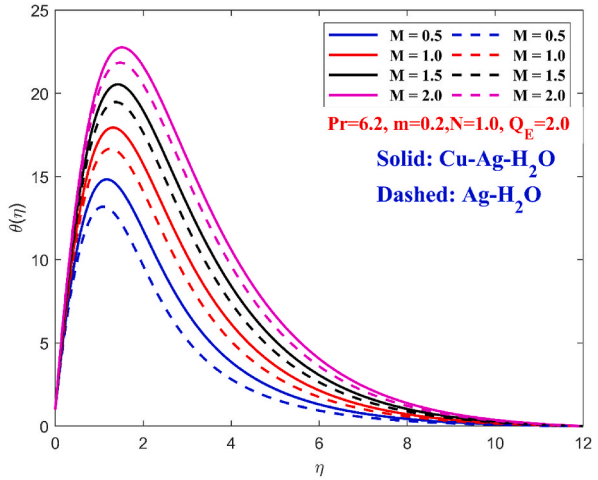

Fig. 4. Outcome of magnetic parameter on temperature.

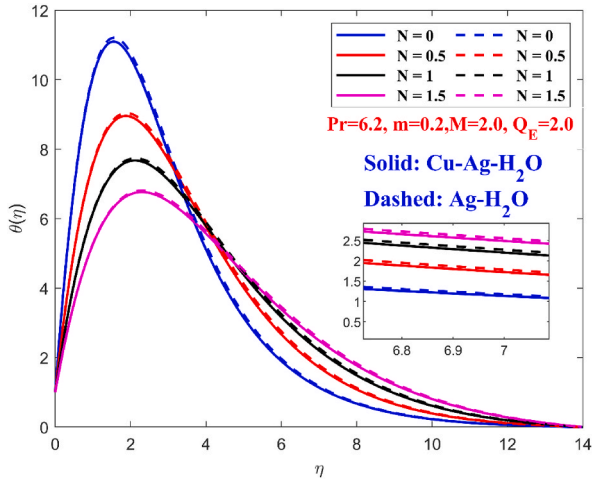

Fig. 5. Outcome of radiation parameter on temperature.

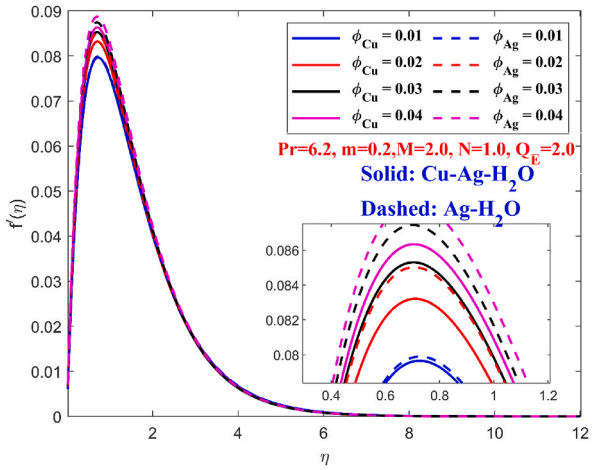

Fig. 6. Outcome of volume fraction on radial velocity.

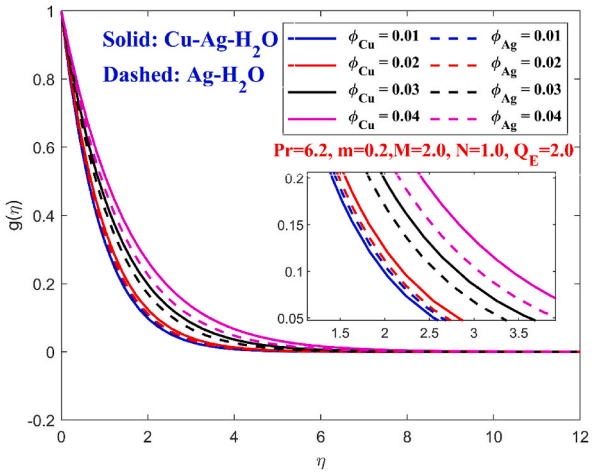

Fig. 7. Outcome of volumetric fraction on cross-radial velocity.

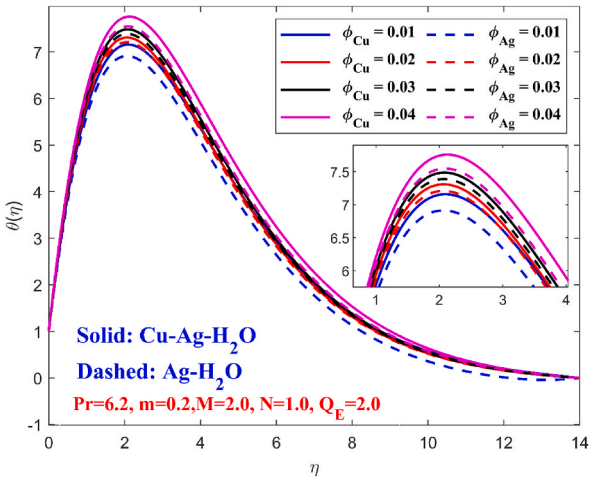

Fig. 8. Outcome of volumetric fraction on temperature.

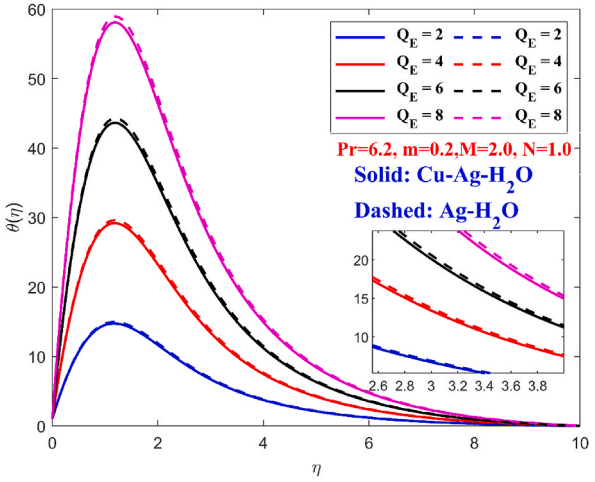

Fig. 9. Outcome of Exponential Heat Source parameter on Temperature.

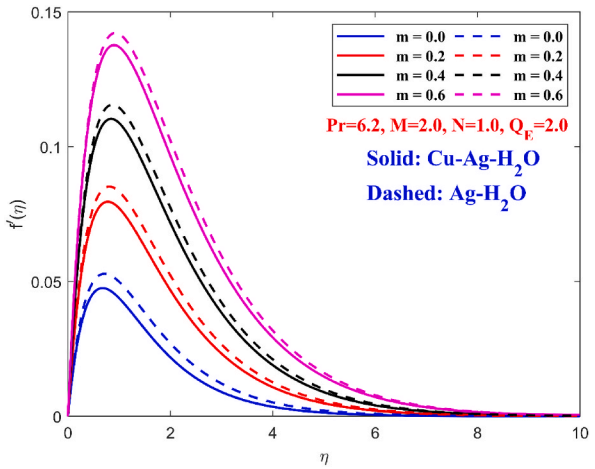

Fig. 10. Outcome of Hall parameter on radial velocity.

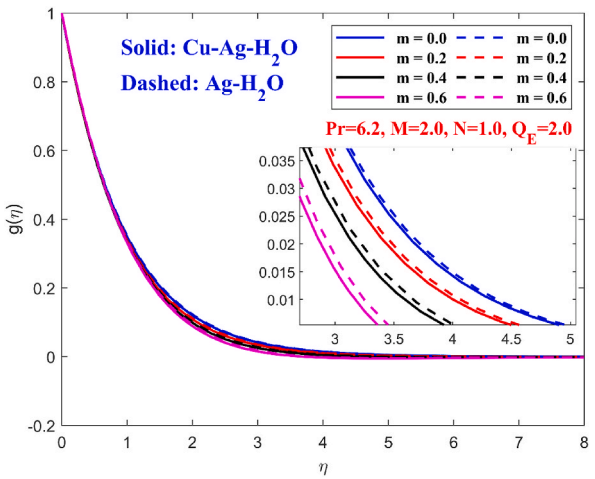

Fig. 11. Outcome of Hall parameter on cross radial velocity.

3. Results and discussion

This section explores the parametric investigation, which aids in understanding the physical perceptions and analyzes the heat transfer characteristics of the presumed fluid model. The influence of the magnetic parameter, thermal radiation, volume fraction, exponential space-dependent source of heat, and hall current parameter on radial velocity, cross-radial velocity, and temperature are explored and exhibited in the form of graphs in Figures (2) to (11). These figures also show the comparative parametric study of the hybrid nanofluid flow ($Cu-Ag-H_2O$) and the nanofluid flow ($Ag-H_2O$). The parameters range in the present model simulation have been assigned as $\varphi_{Cu}=0.02, \varphi_{Ag}=0.02, Q_E=2.0, N=1.0, M=2.0, m=0.2, \mathrm{Pr}=6.2$. The results of the Nusselt number are also estimated and analyzed.

The diminishing radial velocity and transversal (cross-radial) velocities with the rise in magnetic parameter values in both Figs. 2 and 3 can be justified by a retardation force produced by the Lorentz effect along with magnetic field minimizing the velocity naturally. Closer to the surface, the effect becomes insignificant, but in the approximate range of $0 \leq \eta \leq 10$, the same effect is observable and the fluid attains the most enhanced value at $\eta = 1.7$ in Fig. 2 whereas the same effect minimizes in Fig. 3 as the distance from the surface intensifies within the range of $0 \leq \eta \leq 6$. Essentially in both instances, the remarkable performance of nanofluids can be noticed. Calculations from Table 5 are evident for the fall of Cf_r and Cg_r values with the value of a magnetic parameter for both hybrid nanofluids and usual nanofluids justifying that the surface will experience less drag. Hybrid nanofluids continue to showcase the best results as compared to the nanofluids. The escalating temperature due to the positive increase of the magnetic parameter between 0 and 10 is clearly evident in Fig. 4. This is because of the resistance to the retardation force which creates friction between the liquid and the surface originating heat by friction at the level of molecules intensifying the temperature, clearly leading to higher temperatures the $Cu-Ag-H_2O$ than the $Ag-H_2O$. From Table 6 it is observed that, for increasing values of magnetic field parameter, thermal radiation, and heat source parameter values the Nusselt number for both hybrid nanofluid and mono nanofluid is decelerated, while an opposite trend is observed for Hall parameter and volume fraction parameter. Furthermore, the rate of heart transfer is more for the case of hybrid nanofluid in comparison with the case of nanofluid.

Fig. 5 reveals the features of thermal radiation on the temperature of both $Cu-Ag-H_2O$ and $Ag-H_2O$ flows. Initially, the graph depicts that with a rise in the temperature, the parameter of thermal radiation falls but this behavior changes approximately near $\eta = 3.5$ and henceforth the recorded results show a reverse trend. $Cu-Ag-H_2O$ preserves the same behavior trend as $Ag-H_2O$. Noticeably, the presence of radiation causes Brownian mobility at the level of molecules. As a result, the random course of small metals collides with one another. Continuing this molecular situation will typically help the liquid reach its maximum temperature. The inclusion of two particles results in a considerably superior temperature for hybrid colloidal dispersion. Figs. 6 and 7 disclose the behavior of velocities under different volume fraction values of both Cu and Ag nanoparticles. Simulation of hybrid nanofluid is considered by changing the inputs for φ_{Cu} keeping the values of φ_{Ag} fixed. For the simulation of nanofluid, φ_{Cu} is assumed to be zero, regulating the values of φ_{Ag}. The radial velocity amplifies with enhancement in the volumetric fraction values of the nanoparticles. Hence the detectable outcome of the augmented velocity profile of $Cu-Ag-H_2O$ as compared to the $Ag-H_2O$ can be explained in Fig. 6. But the cross-radial velocity diminishes with enhanced volume fractions of the nanoparticles in Fig. 7. It can also be observed that in comparison to the hybrid nanosuspension, the nanosuspension acquires a low-velocity profile. Also, the present simulation

Table 5
Computation of Surface drag for different values of M, m, φ_{Cu}, φ_{Ag}, N, Q_E taking $n = 0.5, \mathrm{Pr} = 6.2$

M	m	N	Q_E	φ_{Cu}	φ_{Ag}	Hybrid Nanofluids ($Cu-Ag-H_2O$)		Nanofluids ($Ag-H_2O$)	
						Cf_r	Cg_r	Cf_r	Cg_r
1.5	0.2	1.0	2.0	0.02	0.02	0.23608035	-0.72725924	0.21445537	-0.68400246
2.0						0.22674181	-0.81887252	0.20643992	-0.77177011
2.5						0.22163398	-0.90317262	0.20225867	-0.85220527
3.0						0.21899467	-0.98120258	0.20029028	-0.92649258
2.0	0.2					0.22674181	-0.81887252	0.20643992	-0.77177011
	0.4					0.29135408	-0.80671350	0.26790316	-0.75934569
	0.6					0.34172552	-0.78284004	0.31579364	-0.73584213
	0.8					0.37650644	-0.75485269	0.34987863	-0.70843276
		0				0.22674181	-0.81887252	0.20643992	-0.77177011
		0.5				0.22674181	-0.81887252	0.20643992	-0.77177011
		1.0				0.22674181	-0.81887252	0.20643992	-0.77177011
		1.5				0.22674181	-0.81887252	0.20643992	-0.77177011
			2			0.22674181	-0.81887252	0.20643992	-0.77177011
			4			0.22674181	-0.81887252	0.20643992	-0.77177011
			6			0.22674181	-0.81887252	0.20643992	-0.77177011
			8			0.22674181	-0.81887252	0.20643992	-0.77177011
				0.01		0.21554790	-0.79462136		
				0.02		0.22674181	-0.81887252		
				0.03		0.23797358	-0.84372894		
				0.04		0.24925633	-0.86921248		
					0.01			0.19444268	-0.74835213
					0.02			0.20643992	-0.77177011
					0.03			0.21844374	-0.79578526
					0.04			0.23046973	-0.82041470

Table 6
Computation of Local heat transfer rate (Nusselt Number) for different values of M, m, φ_{Cu}, φ_{Ag}, N, Q_E taking $n = 0.5, \mathrm{Pr} = 6.2$

M	m	N	Q_E	φ_{Cu}	φ_{Ag}	Hybrid Nanofluids $(Cu - Ag - H_2O)$	Nanofluids $(Ag - H_2O)$
						Nu_r	Nu_r
1.5	0.2	1.0	2.0	0.02	0.02	-22.99227018	-23.08613400
2.0						-24.37348278	-24.42624188
2.5						-25.27363411	-25.30307117
3.0						-25.89393675	-25.90884199
2.0	0.2					-24.37348278	-24.42624188
	0.4					-22.43011938	-22.45368044
	0.6					-20.90022872	-20.91401446
	0.8					-19.67276666	-19.63507203
		0				-20.94767904	-20.99306342
		0.5				-23.15994946	-23.21662699
		1.0				-24.37348278	-24.42624188
		1.5				-25.06766042	-25.11321861
			2			-24.37348278	-24.42624188
			4			-49.70416876	-49.79488949
			6			-75.03485475	-75.16353709
			8			-100.365540	-100.532184
				0.01		-24.41076965	
				0.02		-24.37348278	
				0.03		-24.34044309	
				0.04		-24.31120303	
					0.01		-24.47693365
					0.02		-24.42624188
					0.03		-24.38196270
					0.04		-24.34341077

reveals that the thermal profile amplifies with an intensified volume fraction which is clearly depicted in Fig. 8. This justifies the general belief that the heat energy released by nanoscale particles is greater in $Cu - Ag - H_2O$ than $Ag - H_2O$. As the particles become more minuscule, the amount of heat energy that is produced increases.

Diversified intensities of heat can be channeled into the fluid flow configuration by varying the values of Q_E. From Fig. 9 it can be perceived that the exponential heat source significantly enhances the heat transfer in both the $Cu - Ag - H_2O$ and $Ag - H_2O$ within the range of 0 to 10 whereas the peak temperature is recorded at $\eta = 1.6$ approximately. The conductivity effectively subsides with an increasing hall current parameter reducing the damping impact of the magnetic parameter on the radial velocity, confirming that the increase in radial velocity is due to the increasing worth of the hall parameter in Fig. 10. But on close observation, it can be traced that the velocity is increasing in between the range of 0 to 4 and the peak velocity is recorded slightly away from the surface at $\eta = 1$. Also, it can be perceived that the velocity of the hybrid nanofluid was greater closer to the disk, but an opposing behavior further away from the surface might be acknowledged from Fig. 10. The results demonstrated in Fig. 11, though not so promising, demonstrate reducing cross-radial velocity inside the fluid flow with an enhanced hall parameter. Fig. 12 illustrates that the temperature of both fluids decreases when $0 \leq \eta \leq 12$, in agreement with the far field boundary conditions as the hall parameter increases. Moreover, the $Cu - Ag - H_2O$ has a greater temperature than the $Ag - H_2O$, owing to its higher thermal conductivity.

4. Optimization of surface heat transfer through RSM ~ CCD model

Response Surface Methodology (RSM), a newly established technique in statistics, is hired to determine the ideal response of heat transfer rate for identifying the efficiency of certain factors. The RSM is a sequential process that, depending on the genuine optimum as a point of maximum or lowest, may be compared to climbing a hill or dropping into a valley. The central composite design model is one of the popular models for creating a mathematical representation of a second-order response area. The second-order response surface is model modeled as

$$\Upsilon = \beta_0 + \sum_{i=1}^{3} \beta_i x_i + \sum_{i=1}^{3} \beta_i x_i^2 + \sum_{i=1}^{3} \beta_i \beta_j x_i x_j$$

The above regression model consists of linear effects, quadratic and interaction effects. The current statistical study of the local heat transmission rate (Nusselt number) takes the nanoparticle's volume fraction, the exponential heat source, and thermal radiation into account. Table 7 displays the ranges and the levels the coded symbols (A, B, C) correlate to the (Q_E, N, φ) components required to calculate the Nusselt number's reaction. The simulation procedure has been processed under the permitted range of these parameters and $0.10 \leq Q_E \leq 0.30, 0.5 \leq N \leq 1$ & $0.01 \leq \varphi \leq 0.03$ are considered when calculating the rate of heat transfer. In accordance with the face-centered design method, the CCD's built-in full quadratic model terms such as linear, interaction, and square to develop a second-order model is used. The associated results distribution from 20 independent runs using the multiple settings is displayed in Table 8. Additionally, the full quadratic polynomial provides modeling for the multivariate response function according to the pertinent components as

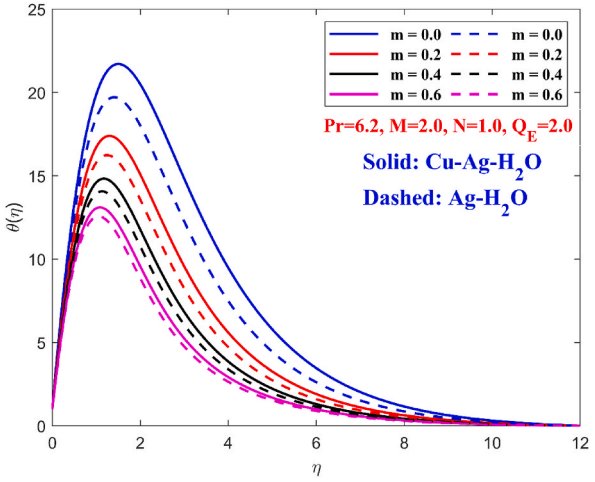

Fig. 12. Outcome of Hall parameter on temperature.

Table 7
Range and levels of independent factors to measure Nusselt number.

Parameter	Level		
	Low (-1)	Middle (0)	High (+1)
$0.10 \leq (A \equiv Q_E) \leq 0.30$	0.10	0.20	0.30
$0.5 \leq (B \equiv N) \leq 1$	0.5	0.75	1
$0.01 \leq (C \equiv \varphi) \leq 0.03$	0.01	0.02	0.03

Table 8
Experimentation design for the Nusselt number.

Runs	Coded Values of the Parameters			Response
	Q_E	N	φ	Nusselt Number
1	0.10(-1)	0.50(-1)	0.01(-1)	-0.38284419
2	0.30(1)	0.50(-1)	0.01(-1)	-2.78821266
3	0.10(-1)	1.00(1)	0.01(-1)	-0.32894901
4	0.30(1)	1.00(1)	0.01(-1)	-2.86703269
5	0.10(-1)	0.50(-1)	0.03(1)	-0.34985287
6	0.30(1)	0.50(-1)	0.03(1)	-2.74598568
7	0.10(-1)	1.00(1)	0.03(1)	-0.29426862
8	0.30(1)	1.00(1)	0.03(1)	-2.82415296
9	0.10(-1)	0.75(0)	0.02(0)	-0.33783635
10	0.30(1)	0.75(0)	0.02(0)	-2.81312127
11	0.20(0)	0.50(-1)	0.02(0)	-1.56393706
12	0.20(0)	1.00(1)	0.02(0)	-1.57586539
13	0.20(0)	0.75(0)	0.01(-1)	-1.59750656
14	0.20(0)	0.75(0)	0.03(1)	-1.55900469
15	0.20(0)	0.75(0)	0.02(0)	-1.57547881
16	0.20(0)	0.75(0)	0.02(0)	-1.57547881
17	0.20(0)	0.75(0)	0.02(0)	-1.57547881
18	0.20(0)	0.75(0)	0.02(0)	-1.57547881
19	0.20(0)	0.75(0)	0.02(0)	-1.57547881
20	0.20(0)	0.75(0)	0.02(0)	-1.57547881

$$\begin{aligned}\text{Nusselt number}(Nu_r) = &-1.57548 - 1.23448 \times Q_E - 0.005944 \times N + 0.019128 \times \varphi_{hnf} \\ &+0.000006 \times {Q_E}^2 + 0.005583 \times N^2 - 0.002771 \times {\varphi_{hnf}}^2 \\ &-0.033308 \times Q_E \times N + 0.002179 \times Q_E \times \varphi_{hnf} + 0.000293 \times N \times \varphi_{hnf}\end{aligned}$$

After deleting the irrelevant components from the obtained response function and calculating the coefficients of regression through the Design of Experiments with RSM, we arrive at the following multivariate model. Nusselt number$(Nu_r) = -1.57548 - 1.23448 \times Q_E - 0.005944 \times N + 0.019128 \times \varphi_{hnf} + 0.005583 \times N^2 - 0.002771 \times {\varphi_{hnf}}^2 - 0.033308 \times Q_E \times N + 0.002179 \times Q_E \times \varphi_{hnf}$

Table 9
Analysis of variance for nusselt number.

Source	Coefficients	DoF	Mean Square_ Adjusted	Sum of Squares_ Adjusted	P_Value	F_Value
Model	-1.57548	9	1.6947	15.2523	0.000	671209.32
Linear		3	5.0811	15.2433	0.000	2012437.68
A	-1.23448	1	15.2393	15.2393	0.000	6035723.99
B	-0.005944	1	0.0004	0.0004	0.000	139.92
C	0.019128	1	0.0037	0.0037	0.000	1449.12
Square		3	0.0000	0.0001	0.001	13.40
AxA	0.000006	1	0.0000	0.0000	0.995	0.00
BxB	0.005583	1	0.0001	0.0001	0.000	33.95
CxC	-0.002771	1	0.0000	0.0000	0.016	8.36
2-Way Interaction		3	0.0030	0.0089	0.000	1176.87
AxB	-0.033308	1	0.0089	0.0089	0.000	3515.28
AxC	0.002179	1	0.0000	0.0000	0.003	15.05
BxC	0.000293	1	0.0000	0.0000	0.614	0.27
Error		10	0.0000	0.0000		
Lack-of-Fit		5	0.0000	0.0000	*	*
Pure Error		5	0.0000	0.0000		
Total		19		15.2523		

Model Summary			
S	R-sq	R-sq–pred-	R-sq- adj
0.0015890	100.00%	100.00%	100.00%

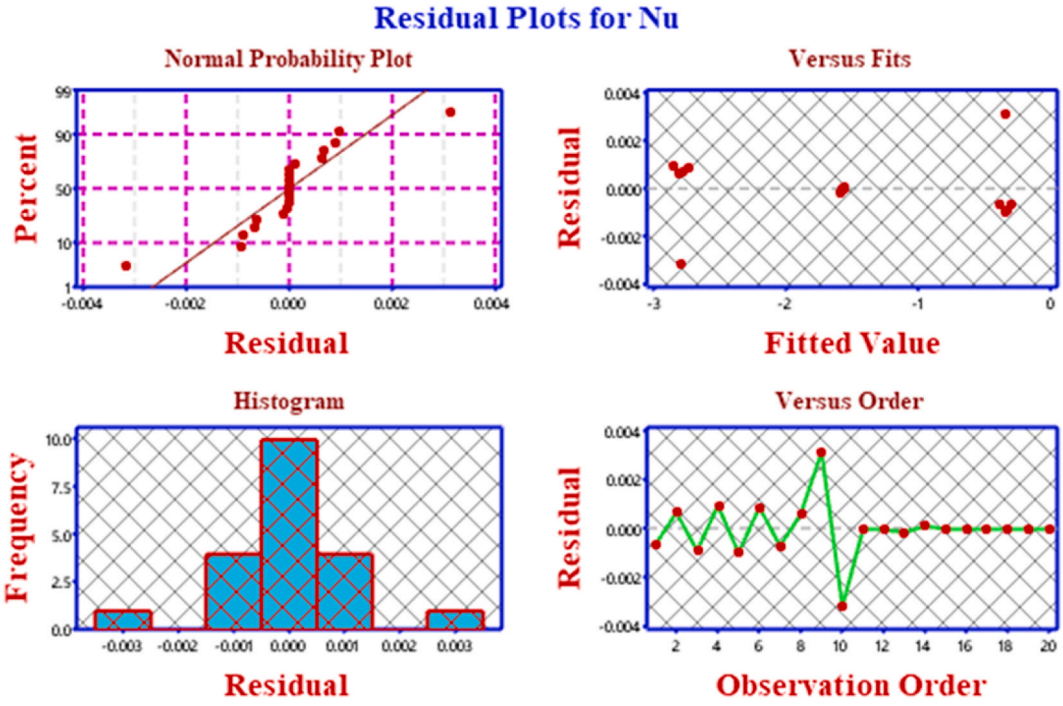

Fig. 13. Residual plots for Nusselt number.

5. Model validity

Utilizing Table 9, Analysis of Variance in short ANOVA, a trustworthy statistical tool is used to evaluate the models of regression and the multiple statistical tests with error, total error, F-values, p-values, and lack of fitting, for the Nusselt number simulation results. The output from the statistical trials on the provided dataset is for achieving a 95% degree of confidence. The suggested Nusselt number regression model's components with p-values larger than 0.05 are removed based on Table 9, yielding the expression that is given in the text. The best-fitting framework for the outcomes has been projected with confidence in its capacity to forecast and optimize based on the calculated values and adjusted values of 100%. The model summary shown in Table 9 corroborates the following:

The distributions of the data for the Nusselt number responses are plotted in Fig. 13 together with the fitting values. The linear

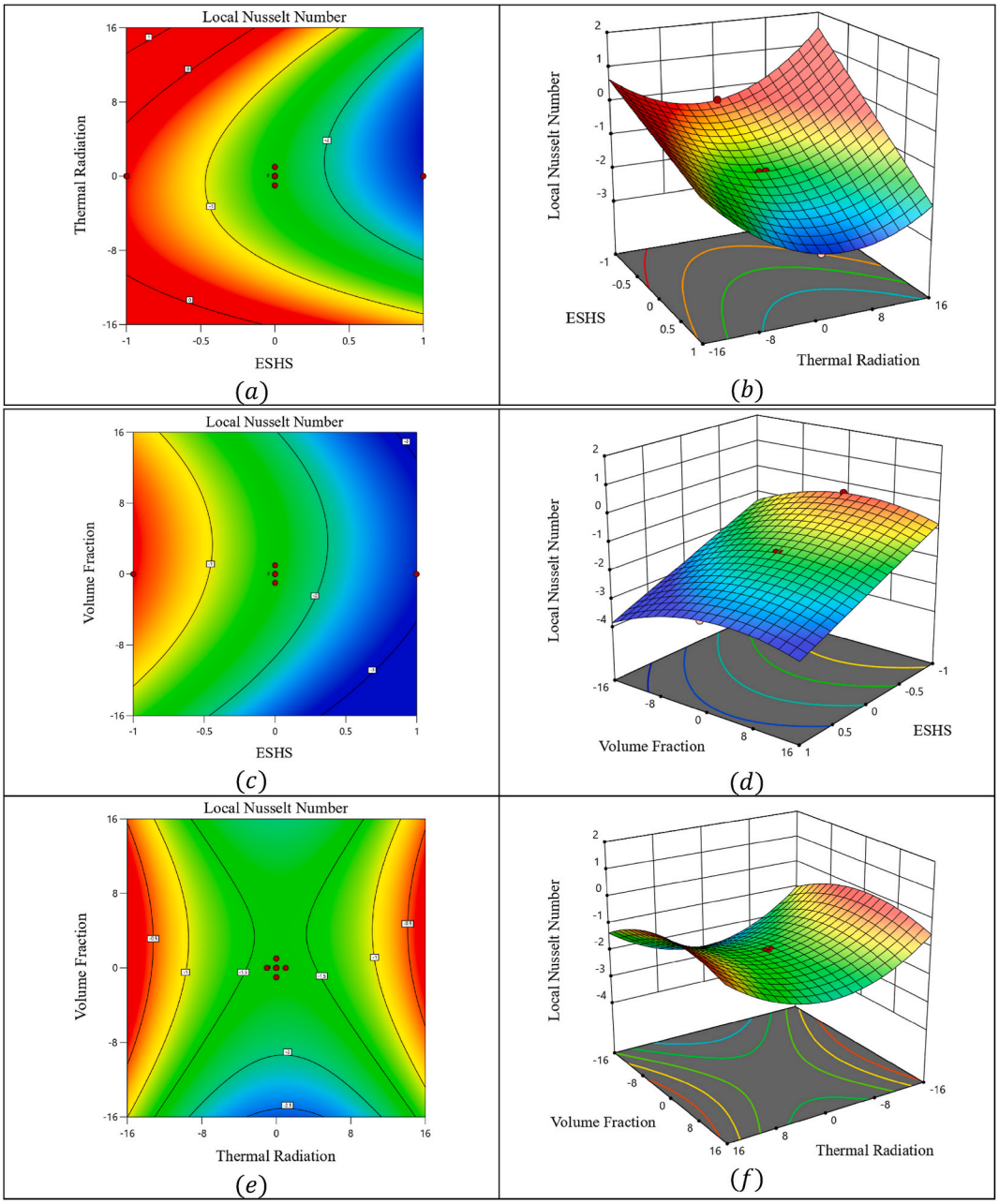

Fig. 14. Contour (a, c, e) and 3D surface (b, d, f) plots for Nu_x

model is an excellent match for these values, as shown by the residuals being near to the straight line, according to the histogram and arrangement of the data in the plot. This demonstrates how the model is suitable for the given data.

Fig. 14(a–f) displays the surface and contour graphs that show how two independent factors (Q_E, N, φ_{hnf}) might affect the heat transfer coefficient while maintaining one of them at a constant middle level. Plots for each independent variable show how the heat transfer coefficient responds to changes in their values. The response function, or Nusselt number, for several potential interaction-independent components, is illustrated by the contour plots (shown in letters a through e) and surface plots (shown in letters b through f). The lines of contour and surface reflections in Fig. 14 (a), (b) respectively are displayed while fixing the Volume fraction (φ_{hnf}) parameter at the central level. The rise in the response function is detected at the lower values of (Q_E). When thermal radiation (N) is increasing from low to high, the local Nusselt number is increasing while an opposite trend is witnessed whenever ESHS (Q_E) is changing from low to high. Figure (c), (d) exemplifies the effect of the interacting factors (φ_{hnf}) and (Q_E) on the local Nusselt number when the intermediate level of N is maintained. The outcomes illustrate that with the independent factor (Q_E) changing from low to higher level values, the response function is decelerating while the higher values of the local Nusselt number are detected at the

middle-level values of (φ_{hnf}) and lower values of (Q_E). Fig. 14 (e), (f) depicts how the factors (N) and (φ_{hnf}) play a part in the variation of the local Nusselt number at an average level of EHS (Q_E). The explored outcomes reveal that the saddle point is observed at the central level values of (N) and (φ_{hnf}). The higher level of (N) and (φ_{hnf}) changing from low to high, contributed significantly to enhancing the rate of heat transfer.

6. Response function sensitivity to independent factors

The purpose of the sensitivity analysis is to explore the impact of tiny parameter variations on the rate of heat transfer. We will be able to learn more about how a small change in one or more factors might affect the efficiency of thermal energy transfer in general by using sensitivity analysis. This approach helps us better understand how minute adjustments to certain parameters might impact how quickly thermal energy is transported, and it also serves as a foundation for future research on the design optimization of systems. The Nusselt number sensitivity, also known as this derivative, indicates how much the Nusselt number is expected to fluctuate in reaction to changing the parameters. Engineers may better understand the heat transfer characteristics related to their designs by using the value of the derivative, which offers useful information about the impact of parameter changes on the Nusselt number. It may be applied to create more effective systems and to enhance current ones. Furthermore, simulation and modeling of the suggested design can deepen our comprehension, allow us to precisely forecast the rate of heat exchange, and help us develop strategies to assure optimum efficacy. The partial derivative of the Nusselt number, also known as coded variables (A, B, C), assesses how sensitive the Nusselt number is to changes in the characterizing factors (Q_E, N, φ_{hnf}).

Using the relevant effective parameters, the partial derivative is calculated as follows:

$$\frac{\partial Nu_r}{\partial Q_E} = -1.23448 - 0.033308N + 0.002179\varphi$$

$$\frac{\partial Nu_r}{\partial N} = -0.005944 + 0.011166N - 0.033308Q_E$$

$$\frac{\partial Nu_r}{\partial \varphi} = 0.019128 - 0.005542\varphi + 0.002179Q_E$$

This graph shows how sensitive the heat transfer rate is to the volume fraction, thermal radiation, and magnetic field parameters in Fig. 15(a) and (b), and 15 (c) respectively. The bars with negative and positive values display, respectively, how the surface rate of heat transmission has decreased and increased. From the Tables, it can be identified that towards all three independent factors, the transmission of heat has the highest sensitivity value (0.024670) towards the volume fraction (φ_{hnf}) *(see* Fig. 15(a)*)* at the middle level of levels of ESHS $(Q_E = 0.20)$. Similarly, the lowest sensitivity value (-1.269967) towards the ESHS (Q_E) parameter *(see* Fig. 15(c)*)* of heat transport is at the coded values of $(A = 0, B = 1, C = -1) Q_E = 0.20, N = 1.0, \varphi_{hnf} = 0.01$ respectively. The sensitivity towards thermal radiation $\left(\frac{\partial Nu_r}{\partial Q_E}\right)$ is diminished when radiative heat flux (N) is changing from low to higher level values, while $\left(\frac{\partial Nu_r}{\partial Q_E}\right)$ an upsurge is when the volume fraction (φ_{hnf}) changes from low to higher level values. Additionally, the lowest value (-1.269967) of sensitivity is observed towards (Q_E) *(see* Fig. 15(c)*)* at the levels of $Q_E = 0.20, N = 1.0, \varphi_{hnf} = 0.01$ and the highest sensitivity value (-1.198993) towards (Q_E) *(see* Fig. 15(a)*)* of heat transmission rate is identified at the uncoded values $Q_E = 0.20, N = 1.0, \varphi_{hnf} = 0.03$. The sensitivity towards thermal radiation $\left(\frac{\partial Nu_r}{\partial N}\right)$ is augmented when radiative heat flux (N) is changing from low to higher level values, while $\left(\frac{\partial Nu_r}{\partial N}\right)$ remains unchanged as the volume fraction (φ_{hnf}) is changing from low to higher level values. Furthermore, the lowest value

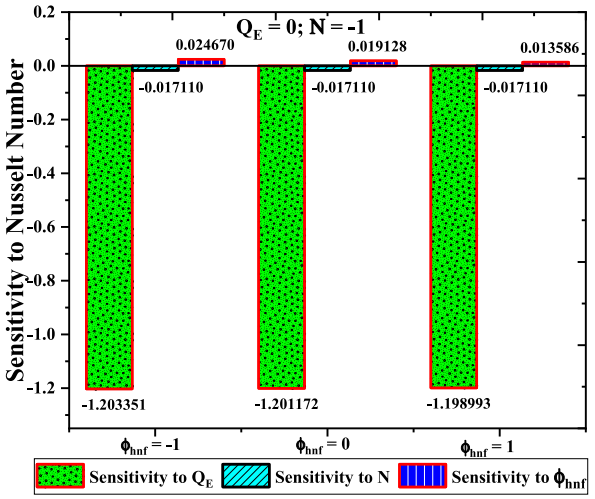

Fig. 15a. The Nusselt number Sensitivity analysis at a Lower level of N

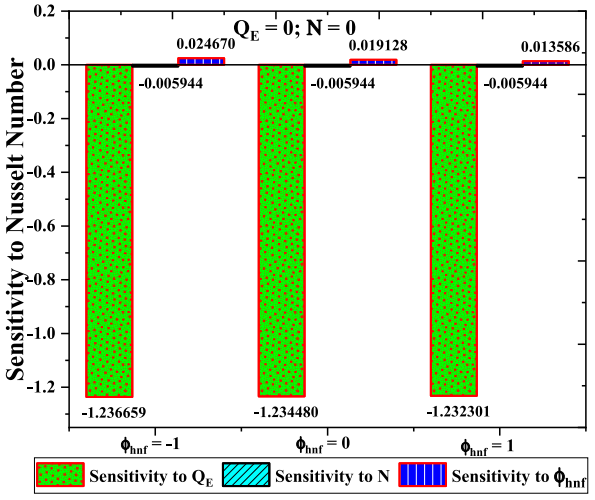

Fig. 15b. The Nusselt number Sensitivity analysis at the Middle level of *N*

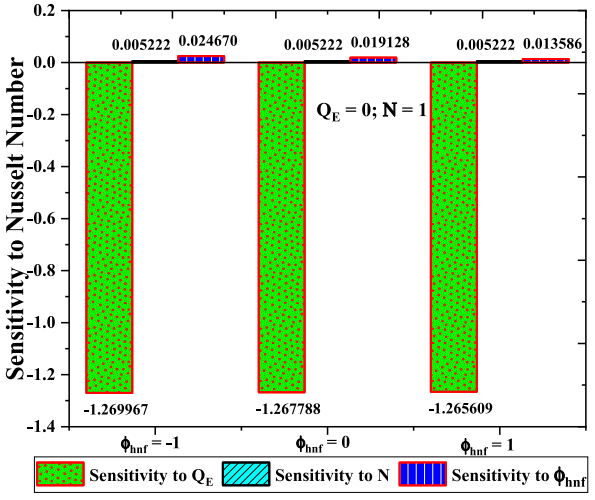

Fig. 15c. The Nusselt number Sensitivity analysis at a Higher level of *N*

(-0.017110) of sensitivity is observed towards thermal radiation *(see* Fig. 15(a)*)* at the levels of $Q_E = 0.20, N = 0.5, \varphi_{hnf} = 0.01$ and the highest sensitivity value (0.005222) towards (N) *(see* Fig. 15(c)*)* of heat transmission rate is obtained at the uncoded values $Q_E = 0.20$, $N = 1.0, \varphi_{hnf} = 0.01$. The sensitivity towards thermal radiation $\left(\frac{\partial Nu_r}{\partial \varphi_{hnf}}\right)$ is augmented when radiative heat flux (N) is changing from low to higher level values, while $\left(\frac{\partial Nu_r}{\partial \varphi_{hnf}}\right)$ remains unchanged as the volume fraction (φ_{hnf}) is changing from low to higher level values. Moreover, the lowest value (0.013586) of sensitivity is observed towards (φ_{hnf}) *(see* Fig. 15(a)*)* at the levels of $Q_E = 0.20, N = 0.5$, $\varphi_{hnf} = 0.01$ and the highest sensitivity value (0.024670) towards (φ_{hnf}) *(see* Fig. 15(c)*)* of heat transmission rate is obtained at the uncoded values $Q_E = 0.20, N = 1.0, \varphi_{hnf} = 0.03$.

7. Conclusions

The prime objective of the current study is the heat transfer analysis of the magnetized flow of $Cu - Ag - H_2O$ and $Ag - H_2O$ radiative flow over a spinning disk when the exponential heat source and hall current are substantial. A complete quadratic CCD framework using the RSM strategy, the sensitivity, and the optimization analysis of the response function (rate of heat transfer) for three independent factors such as the volume fraction, ESHS, and thermal radiation parameters have been performed. The flow governing equations written in partial derivatives are converted to ordinary derivative equations engaging framed similarity transformations and solved numerically using the Runge-Kutta technique. The fluid flow characteristics of magnetic parameter, thermal radiation, volume fraction, exponential space-based heat source, and Hall current parameters are revealed through graphs. Some valuable discrete observations during the exploration of the parameter influence on the flow can be noted as:

- $f'(\eta)$, the radial velocity reduces in the presence of M whereas the same upsurges in the presence of m and (φ_{hnf}). Also, higher velocity is observed for $Ag-H_2O$ than that for $Cu-Ag-H_2O$.
- The cross-radial velocity $g(\eta)$ rises for (φ_{hnf}) and deteriorates for both M and m. Profiles of all parameters discussed displayed maximum velocity for $Ag-H_2O$ than that for $Cu-Ag-H_2O$ making an exception in the case of (φ_{hnf}).
- The temperature $\theta(\eta)$ amplifies enormously for M, Q_E and (φ_{hnf}), but an opposite behavior is observed for m. Results show that $Cu-Ag-H_2O$ acquires maximum temperature when compared to $Ag-H_2O$.
- Hall effect enhances both Cf_r and Cg_r but in comparison the impact is more for $Cu-Ag-H_2O$ than $Ag-H_2O$, also observations show that Cf_r escalates for (φ_{hnf}) whereas Cg_r declines.
- The rate of heat transmission increases with m and (φ_{hnf}) with the optimum effect shown for $Cu-Ag-H_2O$.
- The escalation in the response function is detected at the lower values of (Q_E). When thermal radiation (N) is growing from low to high, the local Nusselt number is also growing while an opposite tendency is witnessed when ESHS (Q_E) is changing from low to high.
- Towards all three independent factors, the transmission of heat has the highest sensitivity value towards the volume fraction (φ_{hnf}) at the middle-level values of $(Q_E = 0.20)$. Also, the lowest sensitivity value towards (Q_E) the parameter of heat transmission is at the coded values of $Q_E = 0.20, N = 1.0, \varphi_{hnf} = 0.01$.

Authorship statement

All persons who meet authorship criteria are listed as authors, and all authors certify that they have participated sufficiently in the work to take public responsibility for the content, including participation in the concept, design, analysis, writing, or revision of the manuscript. Furthermore, each author certifies that this material or similar material has not been and will not be submitted to or published in any other publication before its appearance in the *Case Studies in Thermal Engineering*.

Authorship contributions

The specific contributions made by each author is indicated below:

Conception and design of study: Thirupathi Thumma & Qasem M. Al-Mdallal

Acquisition of data: Devarsu Radha Pyari, Surender Ontela & Fahd Jarad

Analysis and/or interpretation of data: Thirupathi Thumma, Devarsu Radha Pyari, Surender Ontela, Qasem M. Al-Mdallal & Fahd Jarad.

Drafting the manuscript: Thirupathi Thumma, Devarsu Radha Pyari & Surender Ontela

Revising the manuscript critically for important intellectual content: Thirupathi Thumma, Devarsu Radha. Pyari, Surender Ontela, Qasem M. Al-Mdallal & Fahd Jarad.

Declaration of competing interest

None.

Data availability

No data was used for the research described in the article.

Acknowledgements

The authors would like to acknowledge and express their gratitude to the United Arab Emirates University, Al Ain, UAE for providing fnancial support with Grant No. 12S122.

References

[1] S.U.S. Choi, J.A. Eastman, Enhancing thermal conductivity of fluids with nanoparticles, in: Proceedings of the ASME Fluids Engineering Division: International Mechanical Engineering Congress and Exposition, ASME, San Francisco, California, US, 1995, pp. 99–103.

[2] E.A. Algehyne, N.H. Altaweel, A. Saeed, A. Dawar, M. Ramzan, P. Kumam, A semi-analytical passive strategy to examine the water-ethylene glycol (50:50)-based hybrid nanofluid flow over a spinning disk with homogeneous–heterogeneous reactions, Sci. Rep. 12 (2022) 1, https://doi.org/10.1038/s41598-022-21080-z, 2022;12:1–12.

[3] T. Gul, A. Qadeer, W. Alghamdi, A. Saeed, S. Mukhtar, M. Jawad, Irreversibility analysis of the couple stress hybrid nanofluid flow under the effect of electromagnetic field, Int. J. Numer. Methods Heat Fluid Flow 32 (2022) 642–659, https://doi.org/10.1108/HFF-11-2020-0745/FULL/XML.

[4] H. Upreti, A. Mishra, The performance evolution of hybrid nanofluid flow over a rotating disk using Cattaneo–Christov double diffusion and Yamada–Ota model. https://doi.org/10.1080/1745503020222147243, 2022. https://doi.org/10.1080/17455030.2022.2147243.

[5] U. Khan, A. Zaib, I. Waini, A. Ishak, E.S.M. Sherif, W.F. Xia, et al., Impact of Smoluchowski temperature and Maxwell velocity slip conditions on axisymmetric rotated flow of hybrid nanofluid past a porous moving rotating disk, Nanomaterials 12 (2022) 276, https://doi.org/10.3390/NANO12020276, 2022;12:276.

[6] S. Ontela, L. Tlau, Micropolar nanofluid flow in a vertical porous channel: entropy generation analysis, Journal of Applied Nonlinear Dynamics 10 (2021) 305–314, https://doi.org/10.5890/JAND.2021.06.009.

[7] L. Tlau, S. Ontela, Entropy analysis of hybrid nanofluid flow in a porous medium with variable permeability considering isothermal/isoflux conditions, Chin. J. Phys. 80 (2022) 239–252, https://doi.org/10.1016/J.CJPH.2022.10.001.

[8] L. Tlau, S. Ontela, Second law analysis for mixed convection nanofluid flow in an inclined channel with convectively heated walls, Heat Transfer 49 (2020) 1035–1064, https://doi.org/10.1002/HTJ.21652.

[9] T. Thumma, S.N. Satya, Innovations in Eyring–Powell radiative nanofluid flow due to nonlinear stretching sheet with convective heat and mass conditions: numerical study. https://doi.org/10.1080/1448484620201842158, 2020. https://doi.org/10.1080/14484846.2020.1842158.

[10] T. Thumma, S.R. Mishra, Effect of viscous dissipation and joule heating on magnetohydrodynamic jeffery nanofluid flow with and without multi slip boundary conditions, Journal of Nanofluids 7 (2018) 516–526, https://doi.org/10.1166/JON.2018.1469.

[11] M. Khan, W. Ali, J. Ahmed, A hybrid approach to study the influence of Hall current in radiative nanofluid flow over a rotating disk, Appl. Nanosci. 10 (2020) 5167–5177, https://doi.org/10.1007/s13204-020-01415-w.

[12] M.D. Shamshuddin, N. Akkurt, A. Saeed, P. Kumam, Radiation mechanism on dissipative ternary hybrid nanoliquid flow through rotating disk encountered by Hall currents: HAM solution, Alex. Eng. J. (2022), https://doi.org/10.1016/J.AEJ.2022.10.021.

[13] S.A. Shehzad, Z. Abbas, A. Rauf, T. Mushtaq, Effectiveness of Hall current and thermophysical properties in compressible flow of viscous fluid thorough spinning oscillatory disk, Int. Commun. Heat Mass Tran. (2020) 116.

[14] S. Elattar, M.M. Helmi, M.A. Elkotb, M.A. El-Shorbagy, A. Abdelrahman, M. Bilal, et al., Computational assessment of hybrid nanofluid flow with the influence of hall current and chemical reaction over a slender stretching surface, Alex. Eng. J. 61 (2022) 10319–10331, https://doi.org/10.1016/J.AEJ.2022.03.054.

[15] A. Rauf, Faisal, N.A. Shah, T. Botmart, Hall current and morphological effects on MHD micropolar non-Newtonian tri-hybrid nanofluid flow between two parallel surfaces, Sci. Rep. 12 (2022) 1, https://doi.org/10.1038/s41598-022-19625-3, 2022;12:1–20.

[16] Z. Raizah, H. Alrabaiah, M. Bilal, P. Junsawang, A.M. Galal, Numerical study of non-Darcy hybrid nanofluid flow with the effect of heat source and hall current over a slender extending sheet, Sci. Rep. 12 (2022) 1, https://doi.org/10.1038/s41598-022-20583-z, 2022;12:1–12.

[17] M. Ramzan, N. Shahmir, H.A.S. Ghazwani, Hybrid nanofluid flow comprising spherical shaped particles with Hall current and irreversibility analysis: an application of solar radiation. https://doi.org/10.1080/1745503020222123571, 2022. https://doi.org/10.1080/17455030.2022.2123571.

[18] S.M. Mousavi, M. Yousefi, M.N. Rostami, H. Tamim, M. Alimohammadian, S. Dinarvand, Zinc oxide–silver/water hybrid nanofluid flow toward an off-centered rotating disk using temperature-dependent experimental-based thermal conductivity, Heat Transfer 51 (2022) 4169–4186, https://doi.org/10.1002/htj.22494.

[19] I. Waini, A. Ishak, I. Pop, Multiple solutions of the unsteady hybrid nanofluid flow over a rotating disk with stability analysis, Eur. J. Mech. B Fluid 94 (2022) 121–127, https://doi.org/10.1016/J.EUROMECHFLU.2022.02.011.

[20] N. Vijay, K. Sharma, Magnetohydrodynamic hybrid nanofluid flow over a decelerating rotating disk with Soret and Dufour effects, Multidiscip. Model. Mater. Struct. (2022), https://doi.org/10.1108/MMMS-08-2022-0160/FULL/XML ahead-of-print.

[21] N. Acharya, S. Maity, P.K. Kundu, Entropy generation optimization of unsteady radiative hybrid nanofluid flow over a slippery spinning disk, Proc Inst Mech Eng C J Mech Eng Sci 236 (2022) 6007, https://doi.org/10.1177/09544062211065384. –24.

[22] M. Ramzan, S.A. Lone, A. Dawar, A. Saeed, W. Kumam, P. Kumam, Significance of nanoparticle radius and inter-particle spacing toward the radiative water-based alumina nanofluid flow over a rotating disk, Nanotechnol. Rev. 12 (2023), https://doi.org/10.1515/NTREV-2022-0501/ASSET/GRAPHIC/J_NTREV-2022-0501_FIG_015.JPG.

[23] F. Ali, A. Zaib, M.I. Khan, F. Alzahrani, S.M. Eldin, Irreversibility analysis in stagnation point flow of tri-hybrid nanofluid over a rotating disk; application of kinetic energy, J. Indian Chem. Soc. 100 (2023), 100873, https://doi.org/10.1016/J.JICS.2022.100873.

[24] N. Islam, S. Riasat, M. Ramzan, H. Ali S Ghazwani, A. Ali Pasha, S. Kadry, et al., Thermal efficiency appraisal of hybrid nanocomposite flow over an inclined rotating disk exposed to solar radiation with Arrhenius activation energy, Alex. Eng. J. 68 (2023) 721–732, https://doi.org/10.1016/J.AEJ.2022.12.029.

[25] A. Rashid, A. Dawar, M. Ayaz, S. Islam, A.M. Galal, H. Gul, Homotopic solution of the chemically reactive magnetohydrodynamic flow of a hybrid nanofluid over a rotating disk with Brownian motion and thermophoresis effects, ZAMM - Journal of Applied Mathematics and Mechanics/Z. Angew. Math. Mech. (2023), e202200262, https://doi.org/10.1002/ZAMM.202200262.

[26] K. Sarada, F. Gamaoun, A. Abdulrahman, S.O. Paramesh, R. Kumar, G.D. Prasanna, et al., Impact of exponential form of internal heat generation on water-based ternary hybrid nanofluid flow by capitalizing non-Fourier heat flux model, Case Stud. Therm. Eng. 38 (2022), 102332, https://doi.org/10.1016/J.CSITE.2022.102332.

[27] K. Swain, I.L. Animasaun, S.M. Ibrahim, Influence of Exponential Space-Based Heat Source and Joule Heating on Nanofluid Flow over an Elongating/shrinking Sheet with an Inclined Magnetic Field, 43, 2021, https://doi.org/10.1080/01430750.2021.1873854. https://doi.org/10.1080/0143075020211873854, 4045–57.

[28] I. Ullah, Y. Alajlani, A.A. Pasha, M. Adil, W. Weera, Theoretical investigation of hybrid nanomaterials transient flow through variable feature of Darcy–Forchheimer space with exponential heat source and slip condition, Sci. Rep. 12 (2022) 1, https://doi.org/10.1038/s41598-022-17988-1, 2022;12:1–14.

[29] B. Mahanthesh, N.S. Shashikumar, G. Lorenzini, Heat transfer enhancement due to nanoparticles, magnetic field, thermal and exponential space-dependent heat source aspects in nanoliquid flow past a stretchable spinning disk, J. Therm. Anal. Calorim. 145 (2021) 3339–3347, https://doi.org/10.1007/S10973-020-09927-X/METRICS.

[30] B.K. Sharma, A. Kumar, R. Gandhi, M.M. Bhatti, N.K. Mishra, Entropy generation and thermal radiation analysis of EMHD jeffrey nanofluid flow: applications in solar energy, Nanomaterials 13 (2023) 544, https://doi.org/10.3390/NANO13030544, 2023;13:544.

[31] M.D. Shamshuddin, Rajput GovindR, S.R. Mishra, S.O. Salawu, Radiative and exponentially space-based thermal generation effects on an inclined hydromagnetic aqueous nanofluid flow past thermal slippage saturated porous media. http://doi.org/10.1142/S0217979223502028, 2023. https://doi.org/10.1142/S0217979223502028.

[32] K. Ghachem, B. Ahmad, S. Noor, T. Abbas, S.U. Khan, S. Anjum, et al., Numerical simulations for radiated bioconvection flow of nanoparticles with viscous dissipation and exponential heat source, J. Indian Chem. Soc. 100 (2023), 100828, https://doi.org/10.1016/J.JICS.2022.100828.

[33] R.S. Tripathy, P.K. Ratha, S.R. Mishra, Exponential Space-Based Heat Source on Sakiadis Flow of a Dusty Nanofluid Using KKL Model Useful in Solar Radiation, 2023, pp. 1–20, https://doi.org/10.1080/17455030.2023.2168789. http://doi.org/10.1080/1745503020232168789.

[34] S. Jawairia, J. Raza, Optimization of heat transfer rate in a moving porous fin under radiation and natural convection by response surface methodology: sensitivity analysis, Chemical Engineering Journal Advances 11 (2022), 100304, https://doi.org/10.1016/J.CEJA.2022.100304.

[35] M. Alhadri, J. Raza, U. Yashkun, L.A. Lund, C. Maatki, S.U. Khan, et al., Response surface methodology (RSM) and artificial neural network (ANN) simulations for thermal flow hybrid nanofluid flow with Darcy-Forchheimer effects, J. Indian Chem. Soc. 99 (2022), 100607, https://doi.org/10.1016/J.JICS.2022.100607.

[36] A.H. Pordanjani, S.M. Vahedi, F. Rikhtegar, S. Wongwises, Optimization and sensitivity analysis of magneto-hydrodynamic natural convection nanofluid flow inside a square enclosure using response surface methodology, J. Therm. Anal. Calorim. 135 (2019) 1031–1045, https://doi.org/10.1007/S10973-018-7652-6.

[37] A. Shahzad, W.A. Khan, R. Gul, Sensitivity analysis of the nanofluid flow over a stretching flat surface, Pramana - J. Phys. 97 (2023) 1–10, https://doi.org/10.1007/S12043-022-02493-X/METRICS.

[38] T. Mehmood, M. Ramzan, F. Howari, S. Kadry, Y.M. Chu, Application of response surface methodology on the nanofluid flow over a rotating disk with autocatalytic chemical reaction and entropy generation optimization, Sci. Rep. 11 (2021) 1, https://doi.org/10.1038/s41598-021-81755-x, 2021;11:1–18.

[39] P. Rana, J. Mackolil, B. Mahanthesh, T. Muhammad, Cattaneo-Christov Theory to model heat flux effect on nanoliquid slip flow over a spinning disk with nanoparticle aggregation and Hall current. https://doi.org/10.1080/1745503020222048127, 2022. https://doi.org/10.1080/17455030.2022.2048127.

[40] S. Hussain, K. Rasheed, A. Ali, N. Vrinceanu, A. Alshehri, Z. Shah, A sensitivity analysis of MHD nanofluid flow across an exponentially stretched surface with non-uniform heat flux by response surface methodology, Sci. Rep. 12 (2022) 1, https://doi.org/10.1038/s41598-022-22970-y, 2022;12:1–17.

[41] N. Acharya, R. Bag, P.K. Kundu, Influence of Hall current on radiative nanofluid flow over a spinning disk: a hybrid approach, Physica E Low Dimens Syst Nanostruct 111 (2019) 103–112, https://doi.org/10.1016/j.physe.2019.03.006.

[42] H.F. Oztop, E. Abu-Nada, Numerical study of natural convection in partially heated rectangular enclosures filled with nanofluids, Int. J. Heat Fluid Flow 29 (2008) 1326–1336, https://doi.org/10.1016/J.IJHEATFLUIDFLOW.2008.04.009.